

Identifying Clouds over the Pierre Auger Observatory using Infrared Satellite Data

The Pierre Auger Collaboration

P. Abreu⁶¹, M. Aglietta⁴⁹, M. Ahlers⁹⁰, E.J. Ahn⁷⁸, I.F.M. Albuquerque¹⁵, I. Allekotte¹, J. Allen⁸², P. Allison⁸⁴, A. Almela^{11, 7}, J. Alvarez Castillo⁵⁴, J. Alvarez-Muñiz⁷¹, R. Alves Batista¹⁶, M. Ambrosio⁴³, A. Aminaei⁵⁵, L. Anchordoqui⁹¹, S. Andringa⁶¹, T. Antičić²², C. Aramo⁴³, F. Arqueros⁶⁸, H. Asorey¹, P. Assis⁶¹, J. Aublin²⁸, M. Ave⁷¹, M. Avenier²⁹, G. Avila¹⁰, A.M. Badescu⁶⁴, K.B. Barber¹², A.F. Barbosa¹³ ‡, R. Bardenet²⁷, B. Baughman⁸⁴ c, J. Bäuml³³, C. Baus³⁵, J.J. Beatty⁸⁴, K.H. Becker³², A. Bellétoile³¹, J.A. Bellido¹², S. BenZvi⁹⁰, C. Berat²⁹, X. Bertou¹, P.L. Biermann³⁶, P. Billoir²⁸, F. Blanco⁶⁸, M. Blanco²⁸, C. Bleve³², H. Blümer^{35, 33}, M. Boháčová²⁴, D. Boncioli⁴⁴, C. Bonifazi²⁰, R. Bonino⁴⁹, N. Borodai⁵⁹, J. Brack⁷⁶, I. Brancus⁶², P. Brogueira⁶¹, W.C. Brown⁷⁷, P. Buchholz³⁹, A. Bueno⁷⁰, L. Buroker⁹¹, R.E. Burton⁷⁴, M. Buscemi⁴³, K.S. Caballero-Mora^{71, 85}, B. Caccianiga⁴², L. Caccianiga²⁸, L. Caramete³⁶, R. Caruso⁴⁵, A. Castellina⁴⁹, G. Cataldi⁴⁷, L. Cazon⁶¹, R. Cester⁴⁶, S.H. Cheng⁸⁵, A. Chiavassa⁴⁹, J.A. Chinellato¹⁶, J. Chudoba²⁴, M. Cilmo⁴³, R.W. Clay¹², G. Cocciolo⁴⁷, R. Colalillo⁴³, L. Collica⁴², M.R. Coluccia⁴⁷, R. Conceição⁶¹, F. Contreras⁹, H. Cook⁷², M.J. Cooper¹², S. Coutu⁸⁵, C.E. Covault⁷⁴, A. Criss⁸⁵, J. Cronin⁸⁶, A. Curutiu³⁶, R. Dallier^{31, 30}, B. Daniel¹⁶, S. Dasso^{5, 3}, K. Daumiller³³, B.R. Dawson¹², R.M. de Almeida²¹, M. De Domenico⁴⁵, S.J. de Jong^{55, 57}, G. De La Vega⁸, W.J.M. de Mello Junior¹⁶, J.R.T. de Mello Neto²⁰, I. De Mitri⁴⁷, V. de Souza¹⁴, K.D. de Vries⁵⁶, L. del Peral⁶⁹, O. Deligny²⁶, H. Dembinski³³, N. Dhital⁸¹, C. Di Giulio⁴⁴, J.C. Diaz⁸¹, M.L. Díaz Castro¹³, P.N. Diep⁹², F. Diogo⁶¹, C. Dobrigkeit¹⁶, W. Docters⁵⁶, J.C. D'Olivo⁵⁴, P.N. Dong^{92, 26}, A. Dorofeev⁷⁶, J.C. dos Anjos¹³, M.T. Dova⁴, D. D'Urso⁴³, J. Ebr²⁴, R. Engel³³, M. Erdmann³⁷, C.O. Escobar^{78, 16}, J. Espadanal⁶¹, A. Etchegoyen^{7, 11}, P. Facal San Luis⁸⁶, H. Falcke^{55, 58, 57}, K. Fang⁸⁶, G. Farrar⁸², A.C. Fauth¹⁶, N. Fazzini⁷⁸, A.P. Ferguson⁷⁴, B. Fick⁸¹, J.M. Figueira^{7, 33}, A. Filevich⁷, A. Filipčić^{65, 66}, S. Fliescher³⁷, B.D. Fox⁸⁷, C.E. Fracchiolla⁷⁶, E.D. Fraenkel⁵⁶, O. Fratu⁶⁴, U. Fröhlich³⁹, B. Fuchs³⁵, R. Gaior²⁸, R.F. Gamarra⁷, S. Gambetta⁴⁰, B. García⁸, S.T. Garcia Roca⁷¹, D. Garcia-Gamez²⁷, D. Garcia-Pinto⁶⁸, G. Garilli⁴⁵, A. Gascon Bravo⁷⁰, H. Gemmeke³⁴, P.L. Ghia²⁸, M. Giller⁶⁰, J. Gitto⁸, C. Glaser³⁷, H. Glass⁷⁸, G. Golup¹, F. Gomez Albarracin⁴, M. Gómez Berisso¹, P.F. Gómez Vitale¹⁰, P. Gonçalves⁶¹, J.G. Gonzalez³⁵, B. Gookin⁷⁶, A. Gorgi⁴⁹, P. Gorham⁸⁷, P. Gouffon¹⁵, S. Grebe^{55, 57}, N. Griffith⁸⁴, A.F. Grillo⁵⁰, T.D. Grubb¹², Y. Guardincerri³, F. Guarino⁴³, G.P. Guedes¹⁷, P. Hansen⁴, D. Harari¹, T.A. Harrison¹², J.L. Harton⁷⁶, A. Haungs³³, T. Hebbeker³⁷, D. Heck³³, A.E. Herve¹², G.C. Hill¹², C. Hojvat⁷⁸, N. Hollon⁸⁶, V.C. Holmes¹², P. Homola⁵⁹, J.R. Hörandel^{55, 57}, P. Horvath²⁵, M. Hrabovsky^{25, 24}, D. Huber³⁵, T. Huege³³, A. Insolia⁴⁵, S. Jansen^{55, 57}, C. Jarne⁴, S. Jiraskova⁵⁵, M. Josebachuili^{7, 33}, K. Kadija²², K.H. Kampert³², P. Karhan²³, P. Kasper⁷⁸, I. Katkov³⁵, B. Kégl²⁷, B. Keilhauer³³, A. Keivani⁸⁰, J.L. Kelley⁵⁵, E. Kemp¹⁶, R.M. Kieckhafer⁸¹, H.O. Klages³³, M. Kleifges³⁴, J. Kleinfeller^{9, 33}, J. Knapp⁷², R. Krause³⁷, N. Krohm³², O. Krömer³⁴, D. Kruppke-Hansen³², D. Kuempel³⁷, J.K. Kulbartz³⁸, N. Kunka³⁴, G. La Rosa⁴⁸, D. LaHurd⁷⁴, L. Latronico⁴⁹, R. Lauer⁸⁹, M. Lauscher³⁷, P. Lautridou³¹, S. Le Coz²⁹, M.S.A.B. Leão¹⁹, D. Lebrun²⁹, P. Lebrun⁷⁸, M.A. Leigui de Oliveira¹⁹, A. Letessier-Selvon²⁸, I. Lhenry-Yvon²⁶, K. Link³⁵, R. López⁵¹, A. Lopez Agüera⁷¹, K. Louedec^{29, 27}, J. Lozano Bahilo⁷⁰, L. Lu⁷², A. Lucero^{7, 49}, M. Ludwig³⁵, H. Lyberis^{20, 26}, M.C. Maccarone⁴⁸, C. Macolino²⁸, M. Malacari¹², S. Maldera⁴⁹, J. Maller³¹, D. Mandat²⁴, P. Mantsch⁷⁸, A.G. Mariazzi⁴, J. Marin^{9, 49}, V. Marin³¹, I.C. Mariş²⁸, H.R. Marquez Falcon⁵³, G. Marsella⁴⁷, D. Martello⁴⁷, L. Martin^{31, 30}, H. Martinez⁵², O. Martínez Bravo⁵¹, D. Martraire²⁶, J.J. Masías Meza³, H.J. Mathes³³, J. Matthews⁸⁰, J.A.J. Matthews⁸⁹, G. Matthiae⁴⁴, D. Maurel³³, D. Maurizio^{13, 46}, E. Mayotte⁷⁵, P.O. Mazur⁷⁸, G. Medina-Tanco⁵⁴, M. Melissas³⁵, D. Melo⁷, E. Menichetti⁴⁶, A. Menshikov³⁴, S. Messina⁵⁶, R. Meyhandan⁸⁷, S. Mićanović²², M.I. Micheletti⁶, L. Middendorf³⁷, I.A. Minaya⁶⁸, L. Miramonti⁴², B. Mitrica⁶², L. Molina-Bueno⁷⁰, S. Mollerach¹, M. Monasor⁸⁶, D. Monnier Ragaigne²⁷, F. Montanet²⁹, B. Morales⁵⁴, C. Morello⁴⁹, J.C. Moreno⁴, M. Mostafá⁷⁶, C.A. Moura¹⁹, M.A. Muller¹⁶,

G. Müller³⁷, M. Münchmeyer²⁸, R. Mussa⁴⁶, G. Navarra⁴⁹ ‡, J.L. Navarro⁷⁰, S. Navas⁷⁰,
P. Necasal²⁴, L. Nellen⁵⁴, A. Nelles^{55, 57}, J. Neuser³², P.T. Nhung⁹², M. Niechciol³⁹,
L. Niemietz³², N. Nierstenhoefer³², T. Niggemann³⁷, D. Nitz⁸¹, D. Nosek²³, L. Nožka²⁴,
J. Oehlschläger³³, A. Olinto⁸⁶, M. Oliveira⁶¹, M. Ortiz⁶⁸, N. Pacheco⁶⁹, D. Pakk Selmi-Dei¹⁶,
M. Palatka²⁴, J. Pallotta², N. Palmieri³⁵, G. Parente⁷¹, A. Parra⁷¹, S. Pastor⁶⁷, T. Paul^{91, 83},
M. Pech²⁴, J. Pękala⁵⁹, R. Pelayo^{51, 71}, I.M. Pepe¹⁸, L. Perrone⁴⁷, R. Pesce⁴⁰, E. Petermann⁸⁸,
S. Petrera⁴¹, A. Petrolini⁴⁰, Y. Petrov⁷⁶, C. Pfendner⁹⁰, R. Piegai³, T. Pierog³³, P. Pieroni³,
M. Pimenta⁶¹, V. Pirronello⁴⁵, M. Platino⁷, M. Plum³⁷, V.H. Ponce¹, M. Pontz³⁹, A. Porcelli³³,
P. Privitera⁸⁶, M. Prouza²⁴, E.J. Quel², S. Querschfeld³², J. Rautenberg³², O. Ravel³¹,
D. Ravignani⁷, B. Revenu³¹, J. Ridky²⁴, S. Riggi^{48, 71}, M. Risse³⁹, P. Ristori², H. Rivera⁴²,
V. Rizi⁴¹, J. Roberts⁸², W. Rodrigues de Carvalho⁷¹, I. Rodriguez Cabo⁷¹, G. Rodriguez
Fernandez^{44, 71}, J. Rodriguez Martino⁹, J. Rodriguez Rojo⁹, M.D. Rodríguez-Frías⁶⁹, G. Ros⁶⁹,
J. Rosado⁶⁸, T. Rossler²⁵, M. Roth³³, B. Rouillé-d'Orfeuil⁸⁶, E. Roulet¹, A.C. Rovero⁵,
C. Rühle³⁴, S.J. Saffi¹², A. Saftoiu⁶², F. Salamida²⁶, H. Salazar⁵¹, F. Salesa Greus⁷⁶,
G. Salina⁴⁴, F. Sánchez⁷, C.E. Santo⁶¹, E. Santos⁶¹, E.M. Santos²⁰, F. Sarazin⁷⁵, B. Sarkar³²,
R. Sato⁹, N. Scharf³⁷, V. Scherini⁴², H. Schieler³³, P. Schiffer³⁸, A. Schmidt³⁴, O. Scholten⁵⁶,
H. Schoorlemmer^{55, 57}, J. Schovancova²⁴, P. Schovánek²⁴, F.G. Schröder^{33, 7}, J. Schulz⁵⁵,
D. Schuster⁷⁵, S.J. Sciutto⁴, M. Scuderi⁴⁵, A. Segreto⁴⁸, M. Settimo^{39, 47}, A. Shadkam⁸⁰,
R.C. Shellard¹³, I. Sidelnik¹, G. Sigl³⁸, O. Sima⁶³, A. Śmiałkowski⁶⁰, R. Šmída³³, G.R. Snow⁸⁸,
P. Sommers⁸⁵, J. Sorokin¹², H. Spinka^{73, 78}, R. Squartini⁹, Y.N. Srivastava⁸³, S. Stanić⁶⁶,
J. Stapleton⁸⁴, J. Stasielak⁵⁹, M. Stephan³⁷, M. Straub³⁷, A. Stutz²⁹, F. Suarez⁷,
T. Suomijärvi²⁶, A.D. Supanitsky⁵, T. Šušar²², M.S. Sutherland⁸⁰, J. Swain⁸³, Z. Szadkowski⁶⁰,
M. Szuba³³, A. Tapia⁷, M. Tartare²⁹, O. Taşcau³², R. Tcaciuc³⁹, N.T. Thao⁹², D. Thomas⁷⁶,
J. Tiffenberg³, C. Timmermans^{57, 55}, W. Tkaczyk⁶⁰ ‡, C.J. Todero Peixoto¹⁴, G. Toma⁶²,
L. Tomankova³³, B. Tomé⁶¹, A. Tonachini⁴⁶, G. Torralba Elipse⁷¹, D. Torres Machado³¹,
P. Travnicek²⁴, D.B. Tridapalli¹⁵, E. Trovato⁴⁵, M. Tueros⁷¹, R. Ulrich³³, M. Unger³³,
M. Urban²⁷, J.F. Valdés Galicia⁵⁴, I. Valiño⁷¹, L. Valore⁴³, G. van Aar⁵⁵, A.M. van den Berg⁵⁶,
S. van Velzen⁵⁵, A. van Vliet³⁸, E. Varela⁵¹, B. Vargas Cárdenas⁵⁴, G. Varner⁸⁷, J.R. Vázquez⁶⁸,
R.A. Vázquez⁷¹, D. Veberič^{66, 65}, V. Verzi⁴⁴, J. Vicha²⁴, M. Videla⁸, L. Villaseñor⁵³,
H. Wahlberg⁴, P. Wahrlich¹², O. Wainberg^{7, 11}, D. Walz³⁷, A.A. Watson⁷², M. Weber³⁴,
K. Weidenhaupt³⁷, A. Weindl³³, F. Werner³³, S. Westerhoff⁹⁰, B.J. Whelan⁸⁵, A. Widom⁸³,
G. Wiczorek⁶⁰, L. Wiencke⁷⁵, B. Wilczyńska⁵⁹ ‡, H. Wilczyński⁵⁹, M. Will³³, C. Williams⁸⁶,
T. Winchen³⁷, B. Wundheiler⁷, T. Yamamoto⁸⁶ a, T. Yapici⁸¹, P. Younk^{79, 39}, G. Yuan⁸⁰,
A. Yushkov⁷¹, B. Zamorano Garcia⁷⁰, E. Zas⁷¹, D. Zavrtanik^{66, 65}, M. Zavrtanik^{65, 66}, I. Zaw⁸² d,
A. Zepeda⁵² b, J. Zhou⁸⁶, Y. Zhu³⁴, M. Zimbres Silva^{32, 16}, M. Ziolkowski³⁹

¹ Centro Atómico Bariloche and Instituto Balseiro (CNEA-UNCuyo-CONICET), San Carlos de Bariloche, Argentina

² Centro de Investigaciones en Láseres y Aplicaciones, CITEDEF and CONICET, Argentina

³ Departamento de Física, FCEyN, Universidad de Buenos Aires y CONICET, Argentina

⁴ IFLP, Universidad Nacional de La Plata and CONICET, La Plata, Argentina

⁵ Instituto de Astronomía y Física del Espacio (CONICET-UBA), Buenos Aires, Argentina

⁶ Instituto de Física de Rosario (IFIR) - CONICET/U.N.R. and Facultad de Ciencias Bioquímicas y Farmacéuticas U.N.R., Rosario, Argentina

⁷ Instituto de Tecnologías en Detección y Astropartículas (CNEA, CONICET, UNSAM), Buenos Aires, Argentina

⁸ National Technological University, Faculty Mendoza (CONICET/CNEA), Mendoza, Argentina

⁹ Observatorio Pierre Auger, Malargüe, Argentina

¹⁰ Observatorio Pierre Auger and Comisión Nacional de Energía Atómica, Malargüe, Argentina

¹¹ Universidad Tecnológica Nacional - Facultad Regional Buenos Aires, Buenos Aires, Argentina

¹² University of Adelaide, Adelaide, S.A., Australia

¹³ Centro Brasileiro de Pesquisas Físicas, Rio de Janeiro, RJ, Brazil

¹⁴ Universidade de São Paulo, Instituto de Física, São Carlos, SP, Brazil

¹⁵ Universidade de São Paulo, Instituto de Física, São Paulo, SP, Brazil

¹⁶ Universidade Estadual de Campinas, IFGW, Campinas, SP, Brazil

- ¹⁷ Universidade Estadual de Feira de Santana, Brazil
- ¹⁸ Universidade Federal da Bahia, Salvador, BA, Brazil
- ¹⁹ Universidade Federal do ABC, Santo André, SP, Brazil
- ²⁰ Universidade Federal do Rio de Janeiro, Instituto de Física, Rio de Janeiro, RJ, Brazil
- ²¹ Universidade Federal Fluminense, EEIMVR, Volta Redonda, RJ, Brazil
- ²² Rudjer Bošković Institute, 10000 Zagreb, Croatia
- ²³ Charles University, Faculty of Mathematics and Physics, Institute of Particle and Nuclear Physics, Prague, Czech Republic
- ²⁴ Institute of Physics of the Academy of Sciences of the Czech Republic, Prague, Czech Republic
- ²⁵ Palacky University, RCPTM, Olomouc, Czech Republic
- ²⁶ Institut de Physique Nucléaire d'Orsay (IPNO), Université Paris 11, CNRS-IN2P3, Orsay, France
- ²⁷ Laboratoire de l'Accélérateur Linéaire (LAL), Université Paris 11, CNRS-IN2P3, France
- ²⁸ Laboratoire de Physique Nucléaire et de Hautes Energies (LPNHE), Universités Paris 6 et Paris 7, CNRS-IN2P3, Paris, France
- ²⁹ Laboratoire de Physique Subatomique et de Cosmologie (LPSC), Université Joseph Fourier Grenoble, CNRS-IN2P3, Grenoble INP, France
- ³⁰ Station de Radioastronomie de Nançay, Observatoire de Paris, CNRS/INSU, France
- ³¹ SUBATECH, École des Mines de Nantes, CNRS-IN2P3, Université de Nantes, France
- ³² Bergische Universität Wuppertal, Wuppertal, Germany
- ³³ Karlsruhe Institute of Technology - Campus North - Institut für Kernphysik, Karlsruhe, Germany
- ³⁴ Karlsruhe Institute of Technology - Campus North - Institut für Prozessdatenverarbeitung und Elektronik, Karlsruhe, Germany
- ³⁵ Karlsruhe Institute of Technology - Campus South - Institut für Experimentelle Kernphysik (IEKP), Karlsruhe, Germany
- ³⁶ Max-Planck-Institut für Radioastronomie, Bonn, Germany
- ³⁷ RWTH Aachen University, III. Physikalisches Institut A, Aachen, Germany
- ³⁸ Universität Hamburg, Hamburg, Germany
- ³⁹ Universität Siegen, Siegen, Germany
- ⁴⁰ Dipartimento di Fisica dell'Università and INFN, Genova, Italy
- ⁴¹ Università dell'Aquila and INFN, L'Aquila, Italy
- ⁴² Università di Milano and Sezione INFN, Milan, Italy
- ⁴³ Università di Napoli "Federico II" and Sezione INFN, Napoli, Italy
- ⁴⁴ Università di Roma II "Tor Vergata" and Sezione INFN, Roma, Italy
- ⁴⁵ Università di Catania and Sezione INFN, Catania, Italy
- ⁴⁶ Università di Torino and Sezione INFN, Torino, Italy
- ⁴⁷ Dipartimento di Matematica e Fisica "E. De Giorgi" dell'Università del Salento and Sezione INFN, Lecce, Italy
- ⁴⁸ Istituto di Astrofisica Spaziale e Fisica Cosmica di Palermo (INAF), Palermo, Italy
- ⁴⁹ Istituto di Fisica dello Spazio Interplanetario (INAF), Università di Torino and Sezione INFN, Torino, Italy
- ⁵⁰ INFN, Laboratori Nazionali del Gran Sasso, Assergi (L'Aquila), Italy
- ⁵¹ Benemérita Universidad Autónoma de Puebla, Puebla, Mexico
- ⁵² Centro de Investigación y de Estudios Avanzados del IPN (CINVESTAV), México, Mexico
- ⁵³ Universidad Michoacana de San Nicolas de Hidalgo, Morelia, Michoacan, Mexico
- ⁵⁴ Universidad Nacional Autonoma de Mexico, Mexico, D.F., Mexico
- ⁵⁵ IMAPP, Radboud University Nijmegen, Netherlands
- ⁵⁶ Kernfysisch Versneller Instituut, University of Groningen, Groningen, Netherlands
- ⁵⁷ Nikhef, Science Park, Amsterdam, Netherlands
- ⁵⁸ ASTRON, Dwingeloo, Netherlands
- ⁵⁹ Institute of Nuclear Physics PAN, Krakow, Poland
- ⁶⁰ University of Łódź, Łódź, Poland
- ⁶¹ LIP and Instituto Superior Técnico, Technical University of Lisbon, Portugal

- ⁶² 'Horia Hulubei' National Institute for Physics and Nuclear Engineering, Bucharest- Magurele, Romania
- ⁶³ University of Bucharest, Physics Department, Romania
- ⁶⁴ University Politehnica of Bucharest, Romania
- ⁶⁵ J. Stefan Institute, Ljubljana, Slovenia
- ⁶⁶ Laboratory for Astroparticle Physics, University of Nova Gorica, Slovenia
- ⁶⁷ Institut de Física Corpuscular, CSIC-Universitat de València, Valencia, Spain
- ⁶⁸ Universidad Complutense de Madrid, Madrid, Spain
- ⁶⁹ Universidad de Alcalá, Alcalá de Henares (Madrid), Spain
- ⁷⁰ Universidad de Granada and C.A.F.P.E., Granada, Spain
- ⁷¹ Universidad de Santiago de Compostela, Spain
- ⁷² School of Physics and Astronomy, University of Leeds, United Kingdom
- ⁷³ Argonne National Laboratory, Argonne, IL, USA
- ⁷⁴ Case Western Reserve University, Cleveland, OH, USA
- ⁷⁵ Colorado School of Mines, Golden, CO, USA
- ⁷⁶ Colorado State University, Fort Collins, CO, USA
- ⁷⁷ Colorado State University, Pueblo, CO, USA
- ⁷⁸ Fermilab, Batavia, IL, USA
- ⁷⁹ Los Alamos National Laboratory, Los Alamos, NM, USA
- ⁸⁰ Louisiana State University, Baton Rouge, LA, USA
- ⁸¹ Michigan Technological University, Houghton, MI, USA
- ⁸² New York University, New York, NY, USA
- ⁸³ Northeastern University, Boston, MA, USA
- ⁸⁴ Ohio State University, Columbus, OH, USA
- ⁸⁵ Pennsylvania State University, University Park, PA, USA
- ⁸⁶ University of Chicago, Enrico Fermi Institute, Chicago, IL, USA
- ⁸⁷ University of Hawaii, Honolulu, HI, USA
- ⁸⁸ University of Nebraska, Lincoln, NE, USA
- ⁸⁹ University of New Mexico, Albuquerque, NM, USA
- ⁹⁰ University of Wisconsin, Madison, WI, USA
- ⁹¹ University of Wisconsin, Milwaukee, WI, USA
- ⁹² Institute for Nuclear Science and Technology (INST), Hanoi, Vietnam
- (‡) Deceased
- (a) Now at Konan University
- (b) Also at the Universidad Autonoma de Chiapas on leave of absence from Cinvestav
- (c) Now at University of Maryland
- (d) Now at NYU Abu Dhabi

Abstract

We describe a new method of identifying night-time clouds over the Pierre Auger Observatory using infrared data from the Imager instruments on the GOES-12 and GOES-13 satellites. We compare cloud identifications resulting from our method to those obtained by the Central Laser Facility of the Auger Observatory. Using our new method we can now develop cloud probability maps for the 3000 km² of the Pierre Auger Observatory twice per hour with a spatial resolution of ~ 2.4 km by ~ 5.5 km. Our method could also be applied to monitor cloud cover for other ground-based observatories and for space-based observatories.

Keywords: Ultra-high energy cosmic rays; Pierre Auger Observatory; Extensive air showers; Atmospheric monitoring; Clouds; Satellites.

1. Introduction

The Pierre Auger Observatory is located in the province of Mendoza, Argentina, and covers an area of 3000 km². In its original layout, it detects extensive air showers produced by cosmic rays with two different detectors (right panel of Figure 1): a surface detector (SD) [1] and a fluorescence detector (FD) [2]. The SD consists of 1660 water-Cherenkov stations on a triangular grid with 1.5 km spacing. Each SD station detects secondary particles from the extensive air showers arriving at the ground. The FD system consists of 27 air fluorescence telescopes grouped in 4 FD stations located at the borders of the observatory. They are able to detect fluorescence light on clear nights with low moonlight background (left panel of Figure 1). The fluorescence light is emitted by atmospheric nitrogen through interactions with particles produced during the development of the extensive air showers in the atmosphere. Using the fluorescence light detected by the FD, the longitudinal profile of the extensive air showers can be obtained. The shower profile in turn is used to infer the energy and interaction properties of the primary cosmic ray [3, 4].

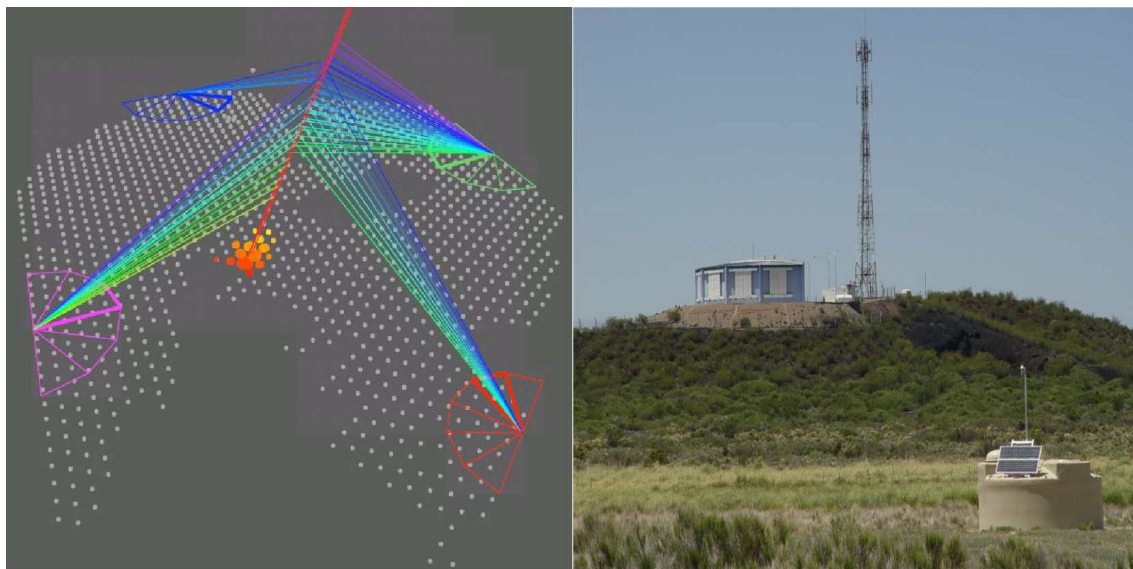


Figure 1: Left: 3D schematic of the Pierre Auger Observatory showing the four FD stations, some SD stations and a cosmic ray event viewed by all four FD stations. Each FD station records the development of the extensive cosmic ray air shower comprised of billions of secondary particles. Right: One of the 1660 SD stations in the foreground and, atop the hill, one of the four FD stations with a communication tower of the Pierre Auger Observatory.

The atmosphere influences many aspects of the generation and detection of extensive air showers. Therefore, an atmospheric group has been formed at the Pierre Auger Observatory [5]. One of the atmospheric factors studied are the clouds. Clouds in the FD aperture can adversely affect the measurement of shower profiles [5]. The Auger Observatory thus routinely employs a number of instruments [6]: the Central Laser Facility (CLF) [7], the eXtended Laser Facility (XLF), LIDARs [8], and IR cameras, to identify clouds over the array. For most cosmic ray studies, the present system is more than adequate [9]. But information from a satellite can complete and enrich the ground measurements. A satellite can cover all the Pierre Auger Observatory area without interfering with the FD acquisition. While LIDARs interfere when scanning inside the FD field of view, introducing a very small dead time. A satellite cloud identification technique would supplement the ground cloud monitoring.

Besides the standard cosmic ray showers, we are also searching for exotic or rare phenomena. The standard cosmic ray air showers have a longitudinal development with a single well-defined shower maximum. However, a small fraction of showers has a profile that differs considerably from this average behavior and could be related to exotic or rare phenomena [10]. For studying such phenomena, we need to rely heavily on well-reconstructed shower profiles (no clouds involved). False exotic profiles may be caused by either absorption of the shower light in clouds or by side-scattering of the longitudinal Cherenkov beam within the clouds. In this way, the sensitivity to such rare events could be enhanced with a night-time cloud monitoring system that covers all the area of the array. This could be a good addition to the methods, listed in the former paragraph, that are employed to identify clouds over the array.

We have developed a method of night-time cloud identification based on infrared-sensitive, geosynchronous satellite observations. In this paper, we describe our method and we use atmospheric monitoring instruments at the observatory as ground truth [11]. We were motivated to do our own cloud identification analysis using the raw satellite data, as the equivalent cloud mask product is not yet freely available.

2. Satellite Data

Our analysis utilizes information provided by the Geostationary Operational Environmental Satellites (GOES) [12]. In particular, we use data from the GOES-12 satellite, which was replaced by GOES-13 in April 2010. The satellite is stationed at 75 degrees West longitude. Its Imager instrument captures images of the South American continent every 30 minutes. Full-hemisphere images are produced in one visible band and four infrared bands, centered at wavelengths 3.9, 6.5, 10.7, and 13.3 μm . These infrared bands are labeled Band 2, Band 3, Band 4 and Band 6 as shown in Figure 2. The bands were chosen to straddle the black-body peak for a typical range of Earth's surface temperatures. In Figure 2, we show these bands superimposed on the calculated emission spectrum for a 280 K black-body at the surface of the Earth, as viewed from space.

The absorption effects of atmospheric water vapor are readily apparent for radiation in Band 3, and to a lesser extent in Band 6. Radiation in Bands 2 and 4 is essentially unaffected by passage through the atmospheric column.

Each pixel in the infrared band has a nadir resolution of 4 km x 4 km. When projected on the ground at the Pierre Auger Observatory, the distance between the center of each pixel is about 2.4 km longitudinally and 5.5 km latitudinally. The pixels become oversampled longitudinally. The location of each pixel within the data stream is completely identified. All information can be separated and reformatted on the ground. Thus, the overlapping regions are removed and only the relevant information for the 2.4 km wide pixel is kept. The visible band resolution is higher.

Each pixel in each wavelength band contains the latitude and longitude of the pixel center and the uncalibrated radiance. Each uncalibrated radiance is subsequently transformed to a calibrated radiance for a particular channel and detector as described by the National Oceanic and Atmospheric Administration - (NOAA) [13].

The archived raw data are publicly available from the NOAA website [14]. For our study, we selected a rectangular region centered at the Pierre Auger Observatory (S 35.6°, W 69.6°). We restricted our analysis to the infrared band data, as we are only interested in night-time cloud cover information. Data for each observation period arrives in 4 binary-formatted files, one for each infrared wavelength band. These files contain information for 539 pixels shown in Figure 3.

We have written analysis routines which read these four binary-formatted files and convert the radiance for each pixel to brightness temperatures T2, T3, T4 and T6. Here the integer labels the corresponding wavelength band. If I_{B_λ} is the measured radiance at a given wavelength λ , then the brightness temperature is given by:

$$T_{B_\lambda} = \left(\frac{hc}{k\lambda} \right) \left(\ln \left(\frac{2hc^2}{I_{B_\lambda} \lambda^5} + 1 \right) \right)^{-1}. \quad (1)$$

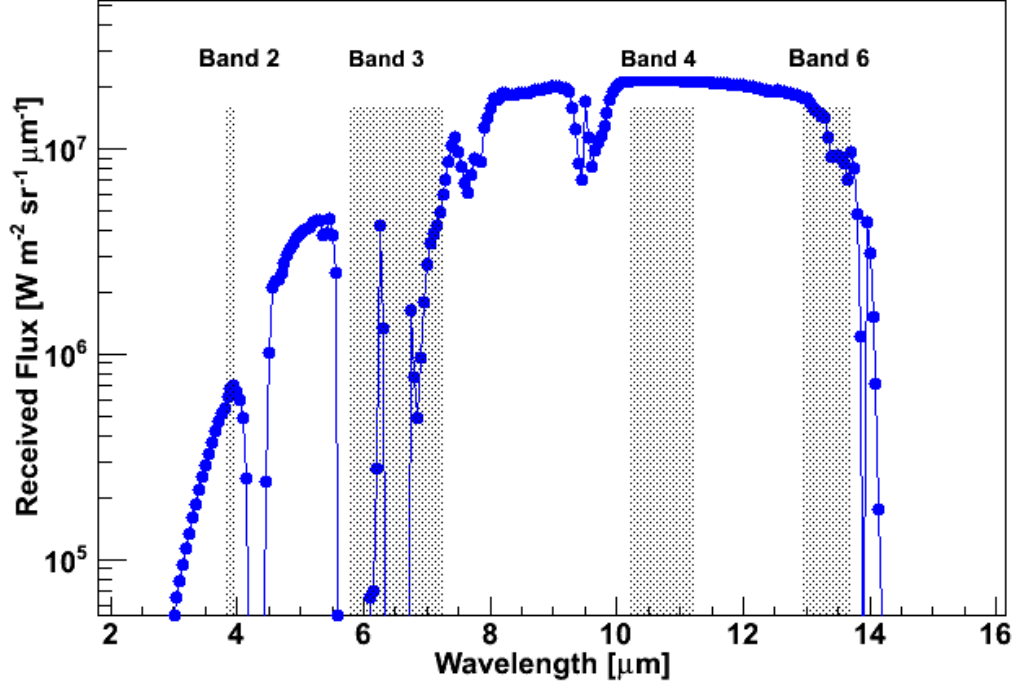


Figure 2: Wavelength band coverage for the GOES-12 Imager, superimposed on the spectrum of a 280 K black-body. Absorption by the atmospheric column has been applied.

Recall that T_{B_λ} should equal the actual temperature T if the emitting surface was a perfect black-body. For real emitting surfaces, the brightness temperature is smaller than the actual temperature, as the measured radiance $I_{B_\lambda} = \epsilon B_\lambda$, where B_λ is the black-body radiance given by the Planck function and ϵ , the emissivity, is less than unity for a real emitting surface. Brightness temperatures thus vary with both the temperature and emissivity of the emitting surface. The brightness temperatures associated with a given pixel are the basic quantities from which cloud determinations are made. The uncertainty for GOES-12 Imager bands is less than 0.2 K at 300 K.

3. Cloud Identification Principles

Clouds are generally colder than the surface of the Earth. Brightness temperatures obtained in the non-absorbing infrared bands, T2 and T4, should consequently be lower for cloud-covered pixels. Precipitous drops in the value of either T2 or T4 should act as an indicator for the presence of a cloud.

Clouds are not pure black-body emitters at infrared wavelengths. Typically, they have low emissivities compared to the nearly black-body emitting Earth. This has the effect of further lowering the measured brightness temperatures T2 and T4 for cloudy pixels.

There is a wavelength dependence in the emissivity of cloud surfaces, which is much greater than that for the surface of the Earth. This dependence arises because the depth into which one can receive radiation from a cloud depends on the relationship between cloud droplet size and wavelength. The quantity T2-T4 is sensitive to emissivity differences between the two bands, but not to the overall temperature, as both T2 and T4 respond to the temperature equivalently. One thus expects T2-T4 to be larger for clouds than for the surface of the Earth.

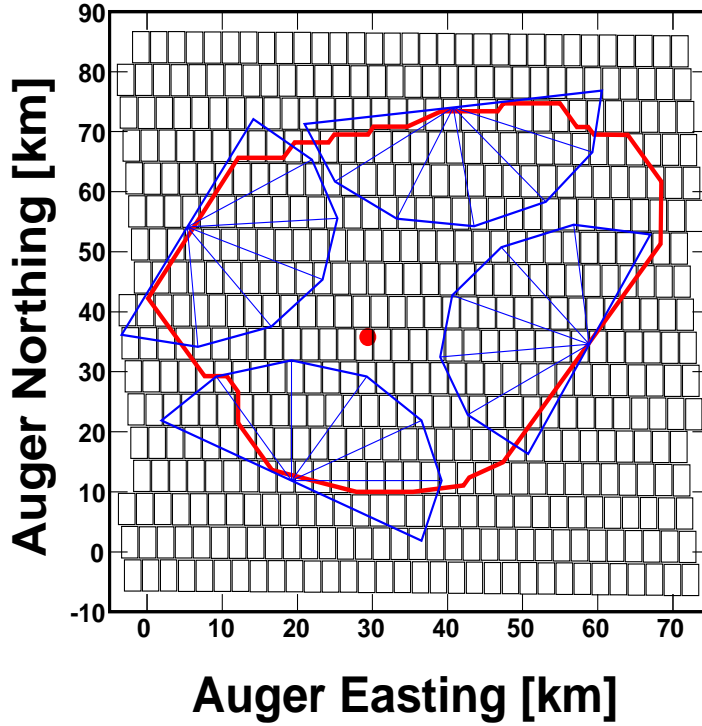


Figure 3: Pixelation of the satellite data. Shown are the borders of the SD (red thick lines), the field of view of the FD telescopes (blue thin lines) and the CLF (red circle). The origin of this map corresponds to 6060000 Northing and 440000 Easting from zone 19 in UTM coordinates.

Considering that clouds consist of a mixture of water vapor and liquid water droplets, clouds can also modulate the absorption of radiation at $6.5 \mu\text{m}$ (Band 3). As we can see in Figure 2, this band is the most sensitive to water vapor. In this way, the brightness temperature T3 can vary with the fraction of cloud in a pixel.

Cloud identification algorithms employing combinations of the brightness temperatures T2, T4 and T3 appear promising.

4. Cloudy/Clear Pixel Tagging with the CLF and FD

It is possible to test the efficacy of the algorithms for cloud identification by checking the cloudy/clear state of the pixel encompassing the CLF (CLF pixel). Every 15 minutes, while the FD operates, the CLF produces a series of 50 vertical laser shots which are observed by all four FD stations. The FD detects the presence of clouds in the vicinity of the CLF as distortions in the otherwise smoothly falling light profiles (blue circles in Figure 4). Clouds immediately above and in the path of the CLF laser beam show up as peaks in the light profiles due to direct scattering, whereas clouds between the FD stations and the CLF show up as dips due to absorption. The latter may not actually be located within the CLF pixel. We ignore clouds identified by dips and include only clouds identified by clearly observed peaks in this study, as they can more unambiguously be compared with satellite measurements of the CLF pixel. A typical CLF vertical laser shot profile indicating the presence of a cloud layer above the CLF is shown in Figure 4 (profile with peak with red stars). The field of view of the FD restricts the maximum height of detected cloud echoes to less than 14 km.

We associate a smooth CLF profile with a “clear CLF” state and a profile containing a peak with a “cloudy CLF” state. We carefully observe each CLF profile and select only those that are

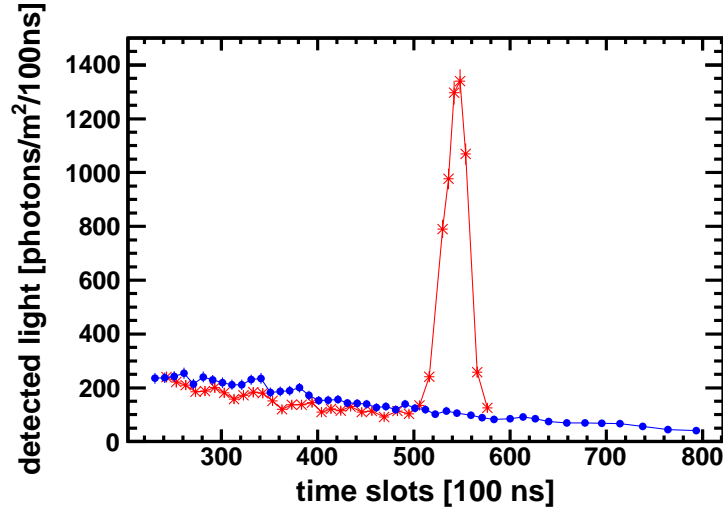


Figure 4: CLF vertical laser profile as seen from the FD station at Los Leones during a clear night (smooth profile with blue circles). A reflection from a cloud layer immediately above the CLF shows up as a peak on the CLF vertical laser profile (red star profile with its peak).

reasonably smooth or contain an obvious peak. We discard the profiles that are difficult to define. Typically, each satellite image is bracketed in time by two CLF shots, one 9 minutes before and the other 6 minutes after the timestamp of the satellite image. The CLF pixel is tagged as “clear CLF pixel” (“cloudy CLF pixel”) if the two bracketing CLF profiles were both identified as “clear CLF” (“cloudy CLF”) states. This is to mitigate the effects of short-term cloud cover changes. The data used in this study were obtained over the period of a year in 2007.

As was mentioned in Section 1, the Pierre Auger Observatory employs three cloud identification instruments: the CLF, the cloud cameras, and the LIDAR system. We chose the CLF to do our ground truth study because its observations best match the geometry and time frame of the satellite observations. Results from the cloud cameras and satellite are not unambiguously comparable as the two devices detect clouds from very different geometric perspectives. The LIDAR system and satellite share some geometric perspective but because of the manner in which the LIDAR data is presently obtained and analyzed observations are not easily matched in time and space.

5. Ground Temperature Correlation

As explained in Section 3, the brightness temperatures T2 and T4 are each equally sensitive to the temperature of most of the emitting surfaces framed by a pixel. For clear pixels, T2 and T4 should be correlated with the temperature of the Earth’s surface. Under clear conditions, the brightness temperature of the ground in these bands is very nearly equal to the actual temperature, as the emissivity of the ground is slightly smaller than unity.

We are able to test this relationship for the CLF pixel, where the ground temperature has been regularly recorded by a weather station installed 2 m above the ground. In Figure 5, we plot values of the brightness temperature T4 of the CLF pixel vs. the ground temperature at the CLF for data taken while the FD was operating in 2007. In this figure, tagged “cloudy CLF pixels” are plotted as red stars and tagged “clear CLF pixels” are designated as open blue circles. There is an evident correlation between brightness temperature and ground temperature for the tagged “clear CLF pixels”. The corresponding fitted line for the tagged “clear CLF pixels” is also shown in Figure 5. The intercept of the line is 38.9 K and the slope is 0.84. This is expected, as the Earth’s surface does not have a perfect unity emissivity.

This combination of satellite and ground observables would make a nice cloud identifier, if the ground temperature were precisely known at each of the ground pixels throughout the array.

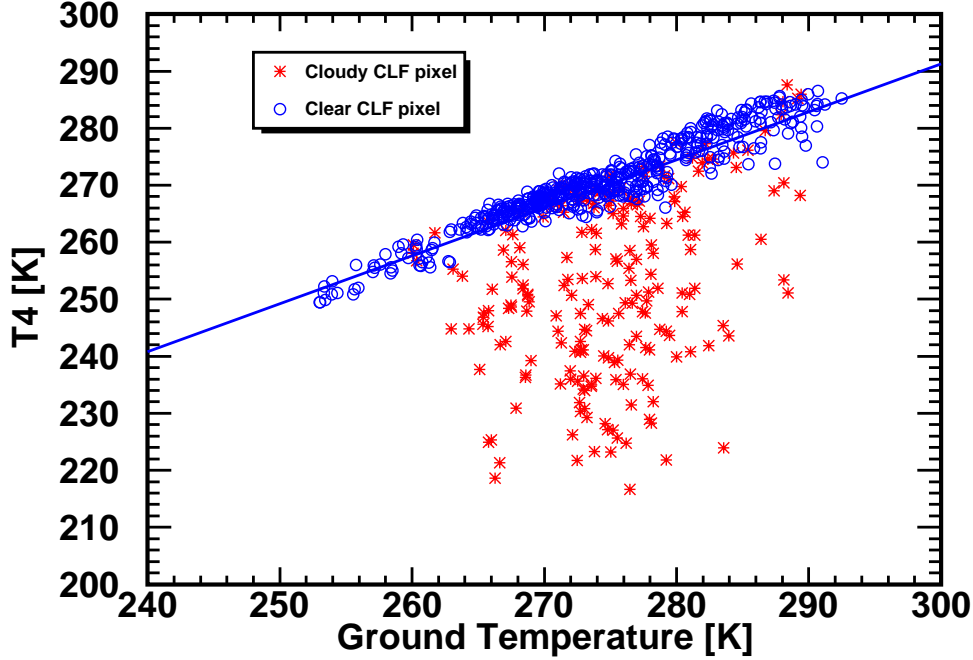


Figure 5: Brightness temperature T_4 vs. ground temperature of the CLF pixel in 2007. Tagged “cloudy CLF pixels” are plotted as red stars and tagged “clear CLF pixels” as open blue circles. The blue line is the fitted line for the tagged “clear CLF pixels”.

Unfortunately, ground temperatures are recorded only at 5 locations within the 3000 km² area. In Figure 5, we can observe that the clear region is very narrow and that there is also a small overlap between the clear and cloudy regions. If we were to use interpolations of the temperature from the 5 locations of the array to infer the temperature for each pixel, we would get larger uncertainties. This might not be a problem for the broader cloudy region, but it would be critical for the clear region and the overlap region. Thus, we proceeded to develop a cloud identification method based on satellite-derived brightness temperatures alone.

6. Satellite-Based Cloud Identification

6.1. Ground-truthing with CLF/FD system

We have identified two satellite-based quantities that appear to distinguish between “clear CLF pixels” and “cloudy CLF pixels”. These are the difference between the two unattenuated brightness temperatures ($T_2 - T_4$) and the highly attenuated brightness temperature (T_3). Both are only mildly dependent on the ground temperature (see Figure 6), minimizing the dependence of our method on seasonal, weekly or daily temperature variations. The use of either satellite-based quantity by itself would appear to do as well at cloud discrimination as the T_4 vs. Ground Temperature method described in Section 5. However, a combination of these quantities should perform even better. In Figure 7, we plot T_3 vs. $T_2 - T_4$ for the CLF pixel data from 2007. The tagged “clear CLF pixels” (open blue circles) congregate in the upper left quadrant of the plot. The tagged “cloudy CLF pixels” (red stars) form an anti-correlated linear feature. The two populations are well-separated when plotted in these variables.

In an effort to maximize the discriminating power of the method we project the data from Figure 7 on to the principal axis X_p defined by a line fitted to the overall distribution. We use

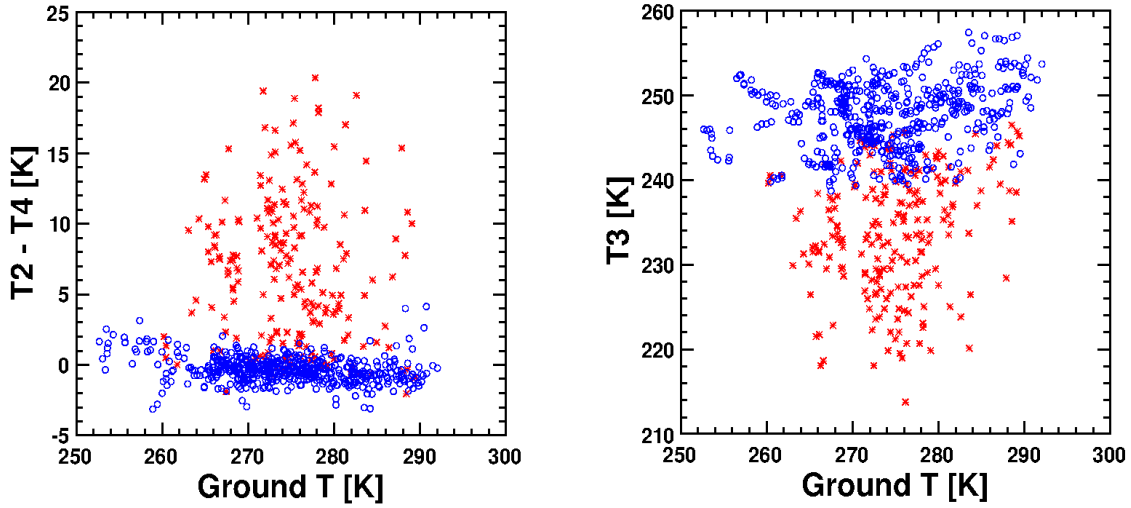


Figure 6: Left: brightness temperature difference ($T_2 - T_4$) vs. ground temperature of the CLF pixel in 2007. Right: Band 3 brightness temperature (T_3) vs. ground temperature of the CLF pixel in 2007. Open blue circles (red stars) were tagged “clear CLF pixels” (“cloudy CLF pixels”) as determined from the CLF study.

the rotation $X_p = (T_2 - T_4) \cos \theta - (T_3 - I_0) \sin \theta$. Here I_0 is the value when $T_2 - T_4 = 0$ for the fitted line in Figure 7, and $\theta = \arctan(m)$, where m is the slope.

On the left of Figure 8, we show one-dimensional histograms of X_p for the clear (black thick line) and cloudy (red dashed line on the right) tagged data. Also shown is a clear pixel “equalized” histogram (blue thin line on the left) scaled to have the same area as the cloudy pixel histogram. Suitably normalized, these histograms represent probability density functions for X_p conditional on the cloudy or clear state of the pixel. Using information from the equalized clear histogram and the cloudy histogram, we calculate a cloud probability for each bin in X_p by dividing the number of cloudy entries by the sum of the cloudy and clear entries. The resulting distribution of cloud probability versus X_p is shown on the right of Figure 8. Also shown is a functional representation of the distribution.

The separation along the principal axis is not perfect. There is a small overlap in the X_p distributions shown on the left panel of Figure 8. We will discuss the possible reasons for the overlap in Subsection 6.3.

6.2. Maps of Cloud Probability and their Application to the Auger Observatory

Based on the cloud identification scheme just described, we have generated a collection of cloud probability maps covering the Pierre Auger Observatory during the course of its operation. In doing this we have assumed that there is nothing special about the CLF pixel in regards to the satellite-based cloud identification algorithm. The cloud probability for each pixel was determined by evaluating the empirical function given in Figure 8 at its particular value of X_p . As an example, a cloud bank moving to the West is shown in the sequence of four cloud probability maps at 30 minute intervals in Figure 9. Cloud probabilities for each pixel are plotted according to the gray scale defined at the right of the cloud probability maps.

Maps were generated for each satellite image available from all the FD running nights since 2004. In general, one image was available every 30 minutes. In addition, nightly animated maps were constructed. These maps (especially the animated versions) are useful in visualizing the cloud cover during and around the occurrence of interesting cosmic ray events. In particular, this helps in distinguishing between cloud-distorted shower profiles and those corresponding to exotic events.

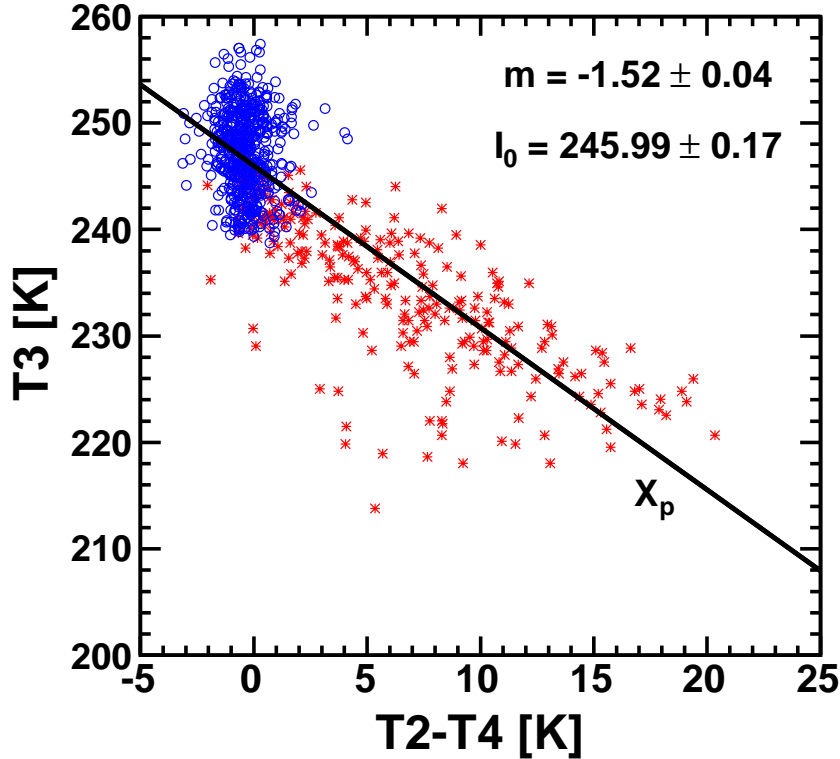


Figure 7: Brightness temperature T_3 vs. brightness temperature difference T_2-T_4 of the CLF pixel in 2007. Open blue circles (red stars) were tagged “clear CLF pixels” (“cloudy CLF pixels”) as determined from the CLF study. I_0 is the value when $T_2-T_4=0$ and m is the slope of the fitted line. X_p is the principal axis of the fitted line.

The array of cloud probabilities and timing information additionally are stored in the Auger GOES database for further reconstruction analysis of the cosmic ray data.

We have developed a simple routine to be used within the Auger offline [15] analysis framework to extract cloud-cover information from the GOES database. At present the code merely extracts the cloud probability for a pixel given a coordinate and a timestamp. In the future we anticipate the development of a more sophisticated routine that will provide the final user with the cloud state of all the pixels between the FD and the shower path. With this information we hope to recover some fraction of the data conservatively thrown away on marginally cloudy nights. We also hope to use it for a fast veto of false exotic events.

The Advanced Data Summary Trees (ADST) files, which are used in high-level Auger data analysis, contain cloud information which comes from the LIDAR systems and recently information from the GOES database and IR cloud cameras has been added.

6.3. Reliability of the method

In the previous section it was pointed out that there exists a small overlap between the X_p distributions for “clear CLF pixels” and “cloudy CLF pixels”. Pixels with X_p falling within the overlap region thus have an ambiguous cloud status. In this section we discuss some possible reasons for this overlap. Since we used a full year of data, this overlap should include almost all the possible cases.

The CLF data and the Satellite images are not obtained simultaneously. They may be offset in time by 6 or 9 minutes. If the cloud cover in the CLF pixel changes significantly on this time scale, the two instruments will inevitably disagree on the cloud status of the pixel. The result

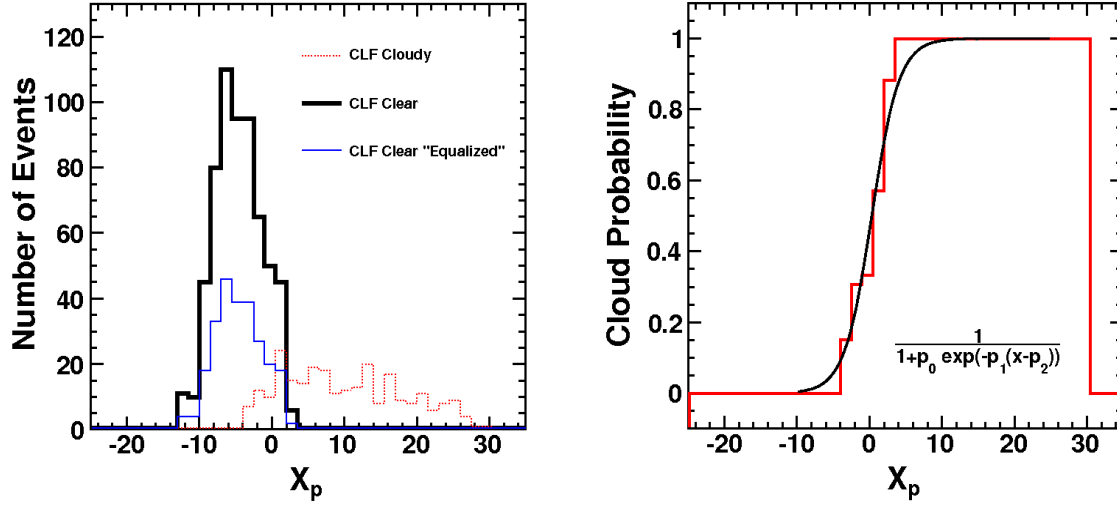


Figure 8: Left: clear (black thick line), clear “equalized” (blue thin line on the left), and cloudy (red dashed line on the right) tagged distributions in rotated (principal axis X_p) system. Right: cloud probability histogram with fitted empirical function.

is a spreading of both clear and cloudy distributions into the intervening region. However, the probability of this is low as we always used satellite images which were time-bracketed by two unchanging CLF measurements.

The overlap region may also result from a spreading of the satellite “cloudy” data into the CLF “clear” distribution. This occurs when the satellite is more cloud-sensitive than the CLF system. This can happen due to the mismatch in geometric perspective between the satellite and CLF system. The CLF laser shots probe the cloudy/clear state of only a small portion of the pixel as seen from the satellite. The laser beam illuminates an area less than 100 m across whereas the pixel itself may measure several kilometers on a side. This effect may be important when the cloud cover is non-uniform but will disappear under overcast conditions. Another contribution may arise from the fact that the field of view of the FD is such that clouds whose bottom surfaces are above 14 km are undetectable by the CLF system. However, clouds at such heights are rare.

We also expect a distribution overlap in cases where the CLF is more cloud-sensitive than the satellite. This is the situation for optically thin clouds. Thin clouds produce a negligible change in the overall infrared flux emitted by a pixel rendering them undetectable by the satellite. Optically thin clouds are not important for distortions due to absorption, but could indeed act as side-scatterers. By averaging the profiles of up to 50 laser shots, the CLF system can readily detect thin-cloud echoes above the night-sky background. The presence of thin clouds have the effect of spreading the satellite “clear” data into the CLF “cloudy” distribution as the CLF detects clouds invisible to the satellite.

In principle, by the above means the CLF/satellite system can discriminate between thin and thick clouds. Thin clouds should frequently be seen by the CLF alone while thick clouds are seen by both monitoring instruments. However the thin clouds detected in this way would have not always a discernible effect on the profiles of single naturally occurring cosmic ray showers as they could only have been detected through the average of many laser-simulated single showers. We would like to remark that our goal is cloud identification and not identification of the cloud type.

As a sanity check for our cloud probabilities, we can inspect our cloud probability maps. For example in Figure 9, we can see that the pixels with high cloud probabilities are continuous and also are commonly surrounded by pixels with lower cloud probabilities.

There is some uncertainty in the ground coordinates of the pixel centers. This uncertainty, if sufficiently large could lead to a mis-identification of the CLF pixel and result in the satellite and

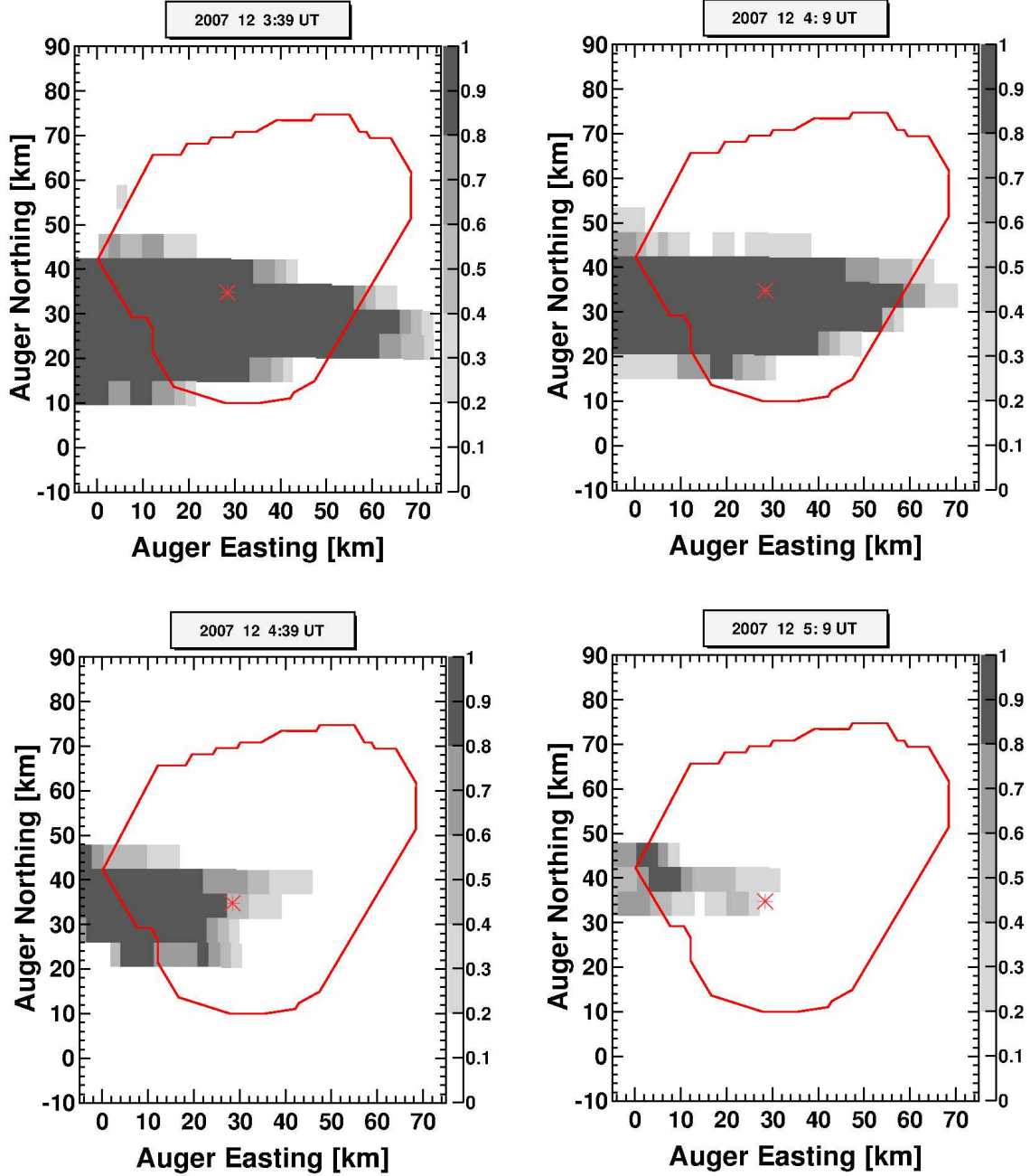


Figure 9: Examples of cloud probability maps. Shown are four successive cloud probability maps of the Pierre Auger Observatory. The progress of a cloud layer can be seen as it moves from East to West. Pixels are colored in accordance with the gray scale to the right of the maps. Shown are the borders of the SD (red) and the location of the CLF (red star).

CLF monitoring the cloud content of two different pixels. The spatial uncertainty in the satellite pixel location could contribute also to the overlap shown on the left panel of Figure 8.

To ascertain the magnitude of the coordinate fluctuations we monitored the position of a known IR point source, the Chaiten Volcano during its eruption in May 2008. The Chaiten Volcano is conveniently located in UTM Zone 18 at 692408 Easting and 5255067 Northing, about 860 km Southwest of the Pierre Auger Observatory. The erupting volcano was identified with the hottest

pixel in maps of the brightness temperature T2. An example of one such map is shown in Figure 10. The volcano appears as a black pixel at the top of the image. The ash plume appears as a much cooler linear feature extending from the volcano pixel to the Southeast.

We were able to identify the hot spot corresponding to the volcano in 45 satellite images from 12 nights. A histogram of the separation between the observed hot spots and the published location of the volcano is displayed in the left panel of Figure 11. The mean displacement of the volcano from its nominal coordinates is about 6 km. Not all of this is attributable to satellite pointing uncertainty as the position of the erupting vent probably changed by several kilometers during the course of the observations. The vent had an equal probability of occurring anywhere within the 2.5 km by 4 km caldera encompassing the volcano. In the right panel of Figure 11 we have histogrammed the two-dimensional locations of the observed hot spots. The hot spot appears to move mainly between two adjacent pixels along a diagonal axis. The caldera happens to be oriented along the same axis. We infer from this that the vent location is fluctuating within the boundaries of the caldera. Given this contribution to the uncertainty of the position of the hot spot, we can only use this study to set an upper limit on the spatial accuracy of the satellite pixels. The accuracy is certainly better than the 6 km figure suggested by this study.

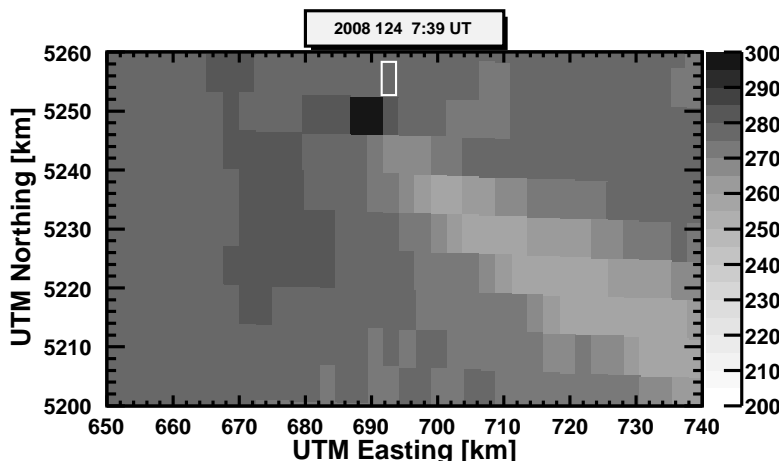


Figure 10: T2 map of the active Chaiten volcano region. The brightness temperature T2 [K] is displayed in gray scale. The red rectangle is the pixel that should encompass the location of the volcano. A displacement of one pixel is apparent in this image.

7. Summary

We have shown that it is possible to calculate the cloud probabilities based on infrared satellite information alone. We expanded this method to assign cloud probabilities to each of the 539 pixels making up the scene based on comparisons between a specific central pixel and ground-based vertical laser shots and under the assumption that the geographical and meteorological conditions of the other 538 pixels are similar to the ones of the central pixel.

As an application of our method, cloud probability maps for the Auger Observatory are generated. These maps are commonly available every 30 minutes during the night.

Our method could be useful for other ground-based and space-based observatories in the region of GOES 12 and GOES 13, specially since the data is publicly available. For observatories in North America the monitoring is even better, since the satellite images are available twice as frequently.

Acknowledgments

The successful installation, commissioning, and operation of the Pierre Auger Observatory would not have been possible without the strong commitment and effort from the technical and

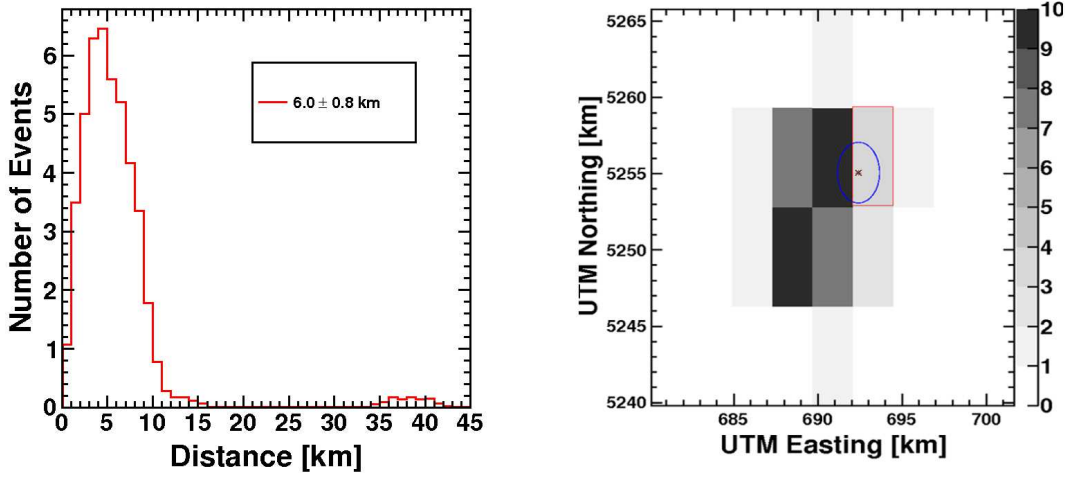


Figure 11: Left: A histogram of the distance between the observed hottest spot and the actual location of the centre of the caldera of the volcano. The mean of the histogram is displayed. For this histogram, each pixel was split into 40 parts with equal area and the caldera was considered as 2.5 km by 4 km. Right: a 2D histogram of the hottest pixel in each of the 44 images is displayed. The mark corresponds to the geographical position of the volcano. The ellipse is a representation of the caldera of the volcano.

administrative staff in Malargüe.

We are very grateful to the following agencies and organizations for financial support: Comisión Nacional de Energía Atómica, Fundación Antorchas, Gobierno De La Provincia de Mendoza, Municipalidad de Malargüe, NDM Holdings and Valle Las Leñas, in gratitude for their continuing cooperation over land access, Argentina; the Australian Research Council; Conselho Nacional de Desenvolvimento Científico e Tecnológico (CNPq), Financiadora de Estudos e Projetos (FINEP), Fundação de Amparo à Pesquisa do Estado de Rio de Janeiro (FAPERJ), Fundação de Amparo à Pesquisa do Estado de São Paulo (FAPESP), Ministério de Ciência e Tecnologia (MCT), Brazil; AVCR AV0Z10100502 and AV0Z10100522, GAAV KJB100100904, MSMT-CR LA08016, LG11044, MEB111003, MSM0021620859, LA08015, TACR TA01010517 and GA UK 119810, Czech Republic; Centre de Calcul IN2P3/CNRS, Centre National de la Recherche Scientifique (CNRS), Conseil Régional Ile-de-France, Département Physique Nucléaire et Corpusculaire (PNC-IN2P3/CNRS), Département Sciences de l'Univers (SDU-INSU/CNRS), France; Bundesministerium für Bildung und Forschung (BMBF), Deutsche Forschungsgemeinschaft (DFG), Finanzministerium Baden-Württemberg, Helmholtz-Gemeinschaft Deutscher Forschungszentren (HGF), Ministerium für Wissenschaft und Forschung, Nordrhein-Westfalen, Ministerium für Wissenschaft, Forschung und Kunst, Baden-Württemberg, Germany; Istituto Nazionale di Fisica Nucleare (INFN), Ministero dell'Istruzione, dell'Università e della Ricerca (MIUR), Italy; Consejo Nacional de Ciencia y Tecnología (CONACYT), Mexico; Ministerie van Onderwijs, Cultuur en Wetenschap, Nederlandse Organisatie voor Wetenschappelijk Onderzoek (NWO), Stichting voor Fundamenteel Onderzoek der Materie (FOM), Netherlands; Ministry of Science and Higher Education, Grant Nos. N N202 200239 and N N202 207238, Poland; Portuguese national funds and FEDER funds within COMPETE - Programa Operacional Factores de Competitividade through Fundação para a Ciência e a Tecnologia, Portugal; Romanian Authority for Scientific Research ANCS, CNDI-UEFISCDI partnership projects nr.20/2012 and nr.194/2012, project nr.1/ASPERA2/2012 ERANET and PN-II-RU-PD-2011-3-0145-17, Romania; Ministry for Higher Education, Science, and Technology, Slovenian Research Agency, Slovenia; Comunidad de Madrid, FEDER funds, Ministerio de Ciencia e Innovación and Consolider-Ingenio 2010 (CPAN), Xunta de Galicia, Spain; The Leverhulme Foundation, Science and Technology Facilities Council, United Kingdom; Department of Energy, Contract Nos. DE-AC02-07CH11359, DE-FR02-04ER41300, DE-FG02-99ER41107,

National Science Foundation, Grant No. 0450696, The Grainger Foundation USA; NAFOSTED, Vietnam; Marie Curie-IRSES/EPLANET, European Particle Physics Latin American Network, European Union 7th Framework Program, Grant No. PIRSES-2009-GA-246806; and UNESCO.

We would like to thank the former Michigan Tech students: Nathan Kelley-Hoskins, Kyle Luck and Arin Nelson for their important contribution to the development of this paper. We would like to thank NOAA for the GOES satellite data that we freely downloaded from their website. Also, we would like to mention in these acknowledgments Dr. Steve Ackerman and Dr. Tony Schreiner for very valuable conversations.

References

- [1] The Pierre Auger Collaboration, I. Allekotte et al., *The Surface Detector system of the Pierre Auger Observatory*, *Nucl. Instrum. Methods* **A 586** (2008) 409-420.
- [2] The Pierre Auger Collaboration, J. Abraham et al., *The Fluorescence Detector of the Pierre Auger Observatory*, *Nucl. Instrum. Methods* **A 620** (2010) 227-251.
- [3] The Pierre Auger Collaboration, J. Abraham et al., *Measurement of the Depth of Maximum of Extensive Air Showers above 10^{18} eV*, *Phys. Rev. Letters* **104** (2010) 091101.
- [4] The Pierre Auger Collaboration, J. Abraham et al., *Measurement of the energy spectrum of cosmic rays above 10^{18} eV using the Pierre Auger Observatory*, *Phys. Letters* **B 685** (2010) 239-246.
- [5] K. Louedec for the Pierre Auger Collaboration, *Atmospheric Monitoring at the Pierre Auger Observatory - Status and Update*, in *Proceedings of the 32nd International Cosmic Ray Conference*, Beijing - China, **2** (2011) 63-66.
- [6] R. Cester et al., *Atmospheric aerosol monitoring at the Pierre Auger Observatory*, in *Proceedings of the 29th International Cosmic Ray Conference*, Pune - India, **8** (2005) 347-350.
- [7] B. Fick et al., *The Central Laser Facility at the Pierre Auger Observatory*, *JINST* **1** (2006) 11003.
- [8] S. BenZvi et al., *The Lidar System of the Pierre Auger Observatory*, *Nucl. Instrum. Methods* **A 574** (2007) 171-184.
- [9] The Pierre Auger Collaboration, J. Abraham et al., *A Study of the Effect of Molecular and Aerosol Conditions in the Atmosphere on Air Fluorescence Measurements at the Pierre Auger Observatory*, *Astroparticle Physics* **33** (2010) 108-129.
- [10] C. Baus et al., *Anomalous Longitudinal Shower Profiles and Hadronic Interactions*, *arXiv:1111.0504 [astro-ph.HE]*.
- [11] J. Chirinos for the Pierre Auger Collaboration, *Ground-truthing a satellite-based night-time cloud identification technique at the Pierre Auger Observatory*, *Eur. Phys. J. Plus* **127** (2012) 93-102.
- [12] GOES Project Science, <http://goes.gsfc.nasa.gov> (accessed December 27th, 2012).
- [13] M. Weinreb et al., *Conversion of GVAR Infrared Data to Scene Radiance or Temperature*, <http://www.oso.noaa.gov/goes/goes-calibration/gvar-conversion.htm> (accessed December 27th, 2012).
- [14] NOAA CLASS, <http://www.class.ncdc.noaa.gov/saa/products/welcome> (accessed December 27th, 2012).
- [15] S. Argirò et al., *The Offline Software Framework of the Pierre Auger Observatory*, *Nucl. Instrum. Methods* **A 580** (2007) 1485-1496.